High-resolution μCT of a mouse embryo using a compact laser-driven X-ray betatron source

Jason M. Cole[a], Daniel R. Symes[b,1], Nelson C. Lopes[a,c], Jonathan C. Wood[a], Kristjan Poder[a], Saleh Alatabi[a], Stanley W. Botchway[b], Peta S. Foster[b], Sarah Gratton[b], Sara Johnson[d], Christos Kamperidis[a,e], Olena Kononenko[f], Michael De Lazzari[g], Charlotte A. J. Palmer[f], Dean Rusby[b], Jeremy Sanderson[h], Michael Sandholzer[h], Gianluca Sarri[i], Zsombor Szoke-Kovacs[d], Lydia Teboul[d], James M. Thompson[g], Jonathan R. Warwick[i], Henrik Westerberg[h], Mark A. Hill[g], Dominic P. Norris[h], Stuart P. D. Mangles[a], and Zulfikar Najmudin[a]

[a]The John Adams Institute for Accelerator Science, Blackett Laboratory, Imperial College London, London SW7 2AZ, United Kingdom; [b]Central Laser Facility, Science and Technology Facilities Council (STFC) Rutherford Appleton Laboratory, Chilton, Didcot OX11 0QX, United Kingdom; [c]Group of Lasers and Plasmas (GoLP)/Instituto de Plasmas e Fusão Nuclear, Instituto Superior Técnico, University of Lisbon, Lisboa 1049-001, Portugal; [d]The Mary Lyon Centre, MRC Harwell Institute, Harwell OX11 0RD, United Kingdom; [e]Extreme Light Infrastructure Attosecond Light Pulse Source (ELI-ALPS), ELI-HU Non-profit Ltd., H-6720 Szeged, Hungary; [f]Linear Accelerator Technologies, Deutsches Elektronen-Synchrotron (DESY), 22607 Hamburg, Germany; [g]Cancer Research UK/Medical Research Council (CRUK/MRC) Oxford Institute for Radiation Research, Gray Laboratories, University of Oxford, Oxford OX3 7DQ, United Kingdom; [h]Medical Research Council (MRC) Harwell Institute, Harwell OX11 0RD, United Kingdom; and [i]School of Mathematics and Physics, Queen's University, Belfast BT7 1NN, United Kingdom

Edited by David A. Weitz, Harvard University, Cambridge, MA, and approved May 9, 2018 (received for review February 9, 2018)

In the field of X-ray microcomputed tomography (μCT) there is a growing need to reduce acquisition times at high spatial resolution (approximate micrometers) to facilitate in vivo and high-throughput operations. The state of the art represented by synchrotron light sources is not practical for certain applications, and therefore the development of high-brightness laboratory-scale sources is crucial. We present here imaging of a fixed embryonic mouse sample using a compact laser–plasma-based X-ray light source and compare the results to images obtained using a commercial X-ray μCT scanner. The radiation is generated by the betatron motion of electrons inside a dilute and transient plasma, which circumvents the flux limitations imposed by the solid or liquid anodes used in conventional electron-impact X-ray tubes. This X-ray source is pulsed (duration <30 fs), bright (>10^{10} photons per pulse), small (diameter <1 μm), and has a critical energy >15 keV. Stable X-ray performance enabled tomographic imaging of equivalent quality to that of the μCT scanner, an important confirmation of the suitability of the laser-driven source for applications. The X-ray flux achievable with this approach scales with the laser repetition rate without compromising the source size, which will allow the recording of high-resolution μCT scans in minutes.

microcomputed tomography | X-ray imaging | laser–plasma acceleration

Compact plasma electron accelerators driven by short-pulse high-power lasers have undergone intensive development since landmark results were published demonstrating the possibility for the production of high-quality electron beams (1–3). This technique, called laser wakefield acceleration (4, 5), has been shown to produce electron beams with unique properties, namely that their size and duration are very small and their charge relatively high. The accelerating fields on the electron bunch are very large, above 100 GV·m^{-1}, and so the required acceleration distance is reduced 1,000-fold compared with conventional electron accelerators. Improvements in laser technology and plasma target design in recent years have driven a steady increase in electron energy and beam quality such that the current generation of petawatt-class laser systems can consistently deliver beams with charge above 100 pC and energy of several gigaelectronvolts in only a few centimeters of plasma (6–9).

Concomitant with the extreme longitudinal acceleration in the wakefield is the emission of an intense short pulse of X-rays, caused by oscillations of the electrons in the transverse plasma electromagnetic fields (10–12). This X-ray radiation, termed betatron radiation, has an ultrashort (<100 fs) pulse duration (13), a low divergence (a few millirads), and a source size of order 1 μm (11, 14). With our current apparatus operating at a repetition rate of 0.05 Hz the average photon flux is ~10^7 photons (ph)·s^{-1} $mrad^{-2}$. The laser systems required to drive these plasma accelerators can be housed in a standard-size laboratory space so it is feasible to deploy the laser-betatron source for a wide range of imaging applications (15) in biomedical science (16–20), material science, and high-energy–density physics (21).

Here we discuss the application of laser-betatron sources to the field of microcomputed tomography (μCT), an established technique for imaging of biological samples (22). X-ray μCT holds the advantages of a spatial resolution superior to magnetic resonance imaging and deeper penetration than optical methods (23, 24). Microfocus sources also have a degree of spatial coherence that enables phase imaging to enhance the contrast between soft tissues of similar X-ray attenuation (25). To demonstrate the effectiveness of laser-betatron μCT we imaged a mouse embryo and compared our results to those of a

Significance

High-resolution microcomputed tomography with benchtop X-ray sources requires long scan times because of the heat load limitation on the anode. We present an alternative, high-brightness plasma-based X-ray source that does not suffer from this restriction. A demonstration of tomography of a centimeter-scale complex organism achieves equivalent quality to a commercial scanner. We will soon be able to record such scans in minutes, rather than the hours required by conventional X-ray tubes.

Author contributions: J.M.C., D.R.S., N.C.L., J.C.W., K.P., S.W.B., P.S.F., S.J., J.S., M.S., L.T., H.W., M.A.H., D.P.N., S.P.D.M., and Z.N. designed research; J.M.C., D.R.S., N.C.L., J.C.W., K.P., S.A., P.S.F., S.G., S.J., C.K., O.K., M.D.L., C.A.J.P., D.R., G.S., Z.S.-K., J.M.T., J.R.W., H.W., M.A.H., S.P.D.M., and Z.N. performed research; J.M.C., N.C.L., J.C.W., K.P., M.D.L., J.M.T., H.W., M.A.H., D.P.N., S.P.D.M., and Z.N. analyzed data; and J.M.C., D.R.S., N.C.L., J.C.W., K.P., M.A.H., D.P.N., S.P.D.M., and Z.N. wrote the paper.

The authors declare no conflict of interest.

This article is a PNAS Direct Submission.

Data Deposition: The data reported in this paper have been deposited on Zenodo (available at https://doi.org/10.5281/zenodo.1255902).

[1]To whom correspondence should be addressed. Email: dan.symes@stfc.ac.uk.

This article contains supporting information online at www.pnas.org/lookup/suppl/doi:10.1073/pnas.1802314115/-/DCSupplemental.

Published online June 5, 2018.

commercial high-resolution μCT scanner routinely used for data collection as part of the International Mouse Phenotyping Consortium (IMPC) (26, 27). Currently, the IMPC estimates that 35% of genes are essential for life, and as such, whole-body 3D embryo imaging, with its ability to visualize abnormal morphology and permit measurements, is critical to reveal the roles that these genes have during embryonic development. To provide a detailed picture of the structural changes that may cause premature death in embryonic lethal mice, a high-throughput imaging platform with micrometer-level resolution is necessary. Benchtop X-ray machines are able to perform fast scans [<15 min (28)] at a resolution of a few micrometers but typically need several hours to maintain image quality at higher resolution (29). We show that with the laser-betatron source, we obtain embryo images of quality equivalent to that of the benchtop scanner but with a single laser pulse rather than the multisecond exposure required with the X-ray tube. In the context of reported results attained with laser-betatron sources, the beams generated here are more than 10 times brighter than those we have previously produced (19) and have a higher photon energy (>10 keV) than used to demonstrate phase-contrast tomography of an insect sample (20). These critical improvements have increased the X-ray penetration depth and improved the image signal-to-noise ratio (SNR), thus enabling 3D reconstruction of a complex centimeter-scale model organism of relevance to human disease studies.

Results

X-Ray Source. The laser-betatron source was generated by focusing high-energy laser pulses into a helium-filled gas cell to generate a plasma, as depicted in Fig. 1. The plasma parameters were tuned to optimize the photon flux and X-ray beam stability, maintaining a consistent energy throughout a scan of several hours and hundreds of X-ray pulses. The accelerator operated in the self-guided, self-injected regime, producing an electron spectrum typically consisting of a high-charge, sub-gigaelectronvolt component and a low-charge, high-energy component extending above 1 GeV (6, 19). The charge in the sub-gigaelectronvolt component (up to 70% of the total) was observed to be correlated with the betatron X-ray flux, so it is likely that this component was responsible for the bulk of the photon emission. The X-ray flux was up to 2.2×10^{10} photons per pulse above 5 keV, in a beam of 10 mrad full-width at half maximum (FWHM) divergence, allowing single-pulse image acquisition with high SNR. For on-shot measurement of the photon energy spectrum during image acquisition, elemental filters were placed in front of the X-ray camera in the corners of the image. To illustrate the penetration of the X-ray beam through biological material we identified a water-equivalent thickness for each metal filter at

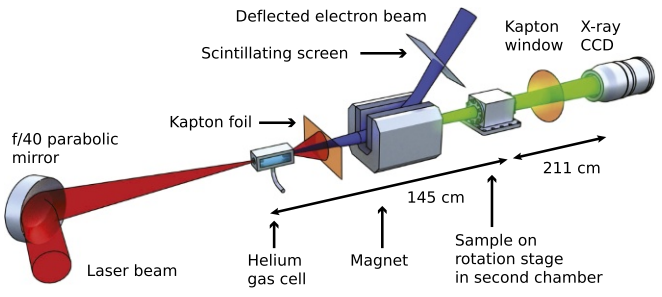

Fig. 1. Schematic of the laser and X-ray beamlines. The laser beam (red) is incident upon a gas cell, producing an electron beam (blue) and an X-ray beam (green). All components are inside a vacuum chamber with the exception of the X-ray camera. The sample is kept at atmospheric pressure inside a secondary chamber.

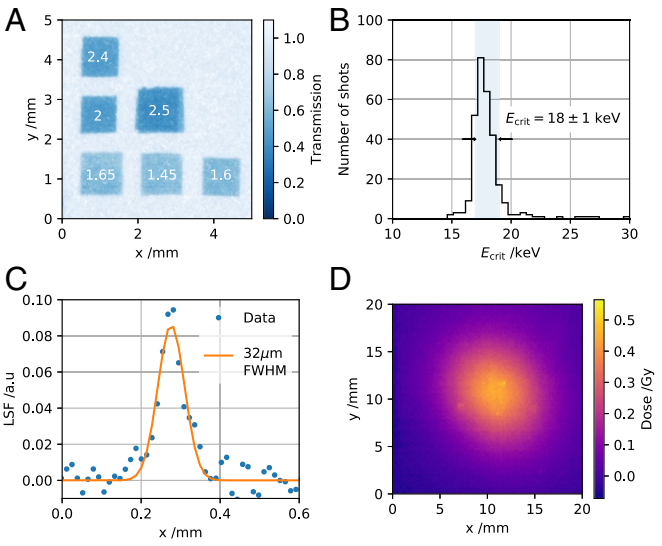

Fig. 2. Characterization of the laser-betatron X-ray beam. (*A*) Measured transmission through metallic filters, with overlaid equivalent thicknesses of water in centimeters at this X-ray energy. (*B*) Distribution of X-ray critical energies E_{crit} recorded during the tomographic scan. (*C*) Measured line-spread function (LSF) of the X-ray detector. (*D*) Integrated X-ray beam dose profile measured at the sample position using EBT3 radiochromic film irradiated with 100 X-ray pulses.

this energy, displayed in Fig. 2*A*). The betatron spectrum is known to resemble that of an on-axis synchrotron spectrum (30), for which we fitted a critical energy $E_{crit} = 18 \pm 1$ keV at the periphery of the beam. The distribution of E_{crit} over the tomographic scan is plotted in Fig. 2*B*, with the 1σ range overlaid. This 6% shot-to-shot jitter in energy is small, enabling a high-quality reconstruction. From spectral measurements taken without a sample present E_{crit} in the center of the beam was found to be ∼25 keV. The betatron X-ray source size can be estimated as ∼1 μm from the value of E_{crit} (*Materials and Methods*).

Imaging Results. The mouse sample was a 14.5-d postcoitum (dpc) embryo of height 10.2 mm stained with potassium triiodide and embedded in agarose. The stain is absorbed at different rates in different tissues, leading to differential photon absorption and generating additional radiographic contrast. When installed inside a sample chamber, the source–sample distance was 1,450 mm and the sample–detector distance was 2,110 mm, giving a geometric magnification of $M = 2.46$. The scintillator resolution (point-spread function FWHM) was measured to be 5.8 pixels, corresponding to 78 μm at the detector or 32 μm at the sample plane (Fig. 2*C*). This is much larger than the X-ray source size and so was the limiting factor on achievable spatial resolution under these conditions.

An example radiograph from a single laser pulse is displayed in Fig. 3*A*, where detector nonuniformities have been subtracted and the spatial profile of the X-ray beam has been accounted for (*Materials and Methods*). Clearly visible are the major contrast-stain–absorbing organs such as the liver, kidneys, and heart. The minimum transmission of the sample is 40%, indicating that the X-ray energy is sufficiently high for such a relatively opaque sample. Importantly, fine features such as the skin, whisker buds, and ribcage are also rendered with clarity and remain well resolved across the image. Fig. 3*B* shows a single projection image taken with the benchtop scanner. Both samples are 14.5-dpc embryos from the same pipeline and as such received equivalent staining and preparation treatment. The laser-betatron image has noticeably higher definition, probably as a consequence of some dehydration leading to larger differences in electron density between

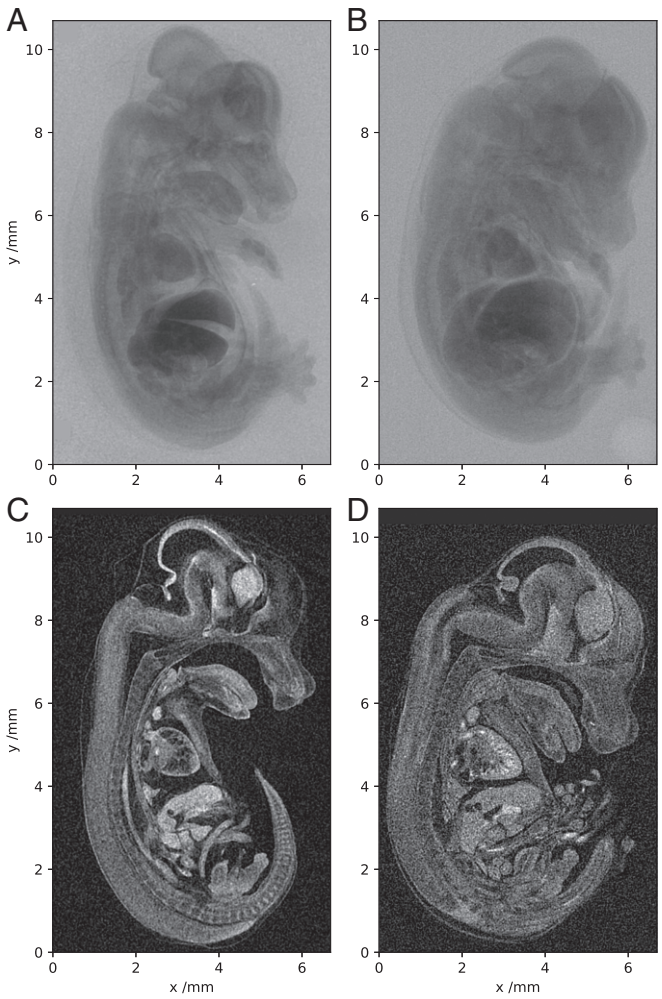

Fig. 3. Tomographic imaging of a 14.5-dpc mouse embryo. (*A*–*D*) Single X-ray projections (*A* and *B*) and sagittal slices from 3D reconstruction (*C* and *D*). *A* and *C* were acquired with the laser-betatron source and *B* and *D* with a commercial microfocus scanner.

the organs and the interorgan spaces. Contrast between adjacent materials might be further increased through propagation-based phase-contrast enhancement since the spatial coherence length at the sample plane is $\sim$100 μm. Critical to the quality of radiography is the SNR of the image, defined as the ratio of the smooth backlighter X-ray signal to the noise magnitude. Before any image processing the local SNR of the radiograph in Fig. 3*A* typically reaches $\approx$20 throughout the region of the image containing the mouse sample. This is well above the lower bound of $\approx$10 for the perception threshold in radiography (31) and ensures that it is possible to visualize features down to the limit set by the detector resolution. After noise removal, the SNR in Fig. 3 *A* and *B* is typically above 100, and qualitatively both projections are observed to be similarly smooth.

Tomography. The sample was rotated through 180° in 0.5° steps to collect a set of projections for tomographic reconstruction. Single images were acquired every 20 s, limited by the laser repetition rate, leading to a scan time of $\sim$2 h. Fiducial wires placed on the edge of the image allowed the correction of any translations of the X-ray source. In Fig. 3 *C* and *D* we compare sagittal slices through the reconstruction obtained with the laser-betatron source with that from the benchtop scanner using the same number of projection images. The same noise-removal process (*Materials and Methods*) was applied to images from the scanner, before reconstruction using the supplied commercial software.

Plotted in Fig. 4 is an isosurface of the laser-betatron reconstruction, cut to visualize a sagittal slice (blue). Fig. 4 *A* and *B* shows orthogonal slices through two volumes of interest, the heart and liver, respectively. It is apparent that fine detail is well preserved in the heart; the internal structure is clearly resolved. Additionally, although the liver shows strong absorption due to increased take-up of the contrast stain, it remains sufficiently transparent that detail is visible throughout and beam-hardening artifacts are not problematic. Alternative animated views of a volume rendering of the reconstruction are available in Movies S1 and S2, the latter rendered at higher transparency for better visibility of the internal structure. Detailed analysis of the tomographic dataset confirmed that the source has sufficient resolution to match the performance of the high-resolution benchtop scanner.

One of the distinctive features of this source is its exceptionally short pulse duration, which would eliminate the problem of motion blur from future applications to live animal imaging. To be viable, the dose for a single tomographic scan must remain below the lethal level, which for an adult mouse is in the range of 5–7.6 Gy, and for longitudinal studies the single-scan dose must remain below several hundred milligrays (32). We measured the average dose using calibrated EBT3 radiochromic film exposed to a series of 100 X-ray pulses. The film confirmed the smooth X-ray beam profile, shown in Fig. 2*D*, and recorded an average dose to a 10×10-mm^2 field of $\approx$0.33 Gy, corresponding to a single-image dose of $\approx$3 mGy. This would therefore allow hundreds of projections at a dosage acceptable for in vivo tomographic scanning.

Discussion

The ability of synchrotron radiation to visualize features at the submicrometer level has been proved in μCT studies of the structure of bones (33, 34), the brain (35), and lungs (36). Moreover, the extreme photon flux of these beamlines allows rapid image acquisition so that fast biological processes such as the beating of insect wings (37) or murine breathing cycle (36) can be resolved. The strong motivation to translate these advanced capabilities to laboratory and clinical environments is driving innovative research to develop compact X-ray technologies. Several products are now on the market with source brightness orders of magnitude higher than that of conventional solid anode X-ray tubes (38, 39). By switching to a liquid anode the electron-beam power can be increased, reducing high-resolution single-image exposure times to of order 1 s, enabling few minute long μCT scans (38). An alternative technique uses inverse Compton scattering of a laser pulse from a high-energy electron bunch to generate narrow bandwidth X-rays that have been used for phase-contrast μCT of biological samples (40) with recent work demonstrating exposure times as short as 50 ms (41). However, with these sources, shorter exposure times come at the cost of a reduction in SNR. A challenge therefore remains to match the exceptional resolution and image quality of a synchrotron beamline at the fast acquisition rate necessary for in vivo imaging and high-throughput scanning.

The laser-betatron source has a combination of properties that are ideally suited for this task: short pulse duration, micrometer X-ray source size, and extreme brightness. Delivery of $\sim 10^{10}$ photons within $<$100 fs means that the good SNR can be maintained at a high frame rate. The spectrum is controllable by changing the plasma conditions and unlike X-ray tube sources the accelerator can be operated at higher average power to increase the average photon flux without increasing the source size and compromising the image resolution. As an example of imaging capability we demonstrated μCT of a murine embryo.

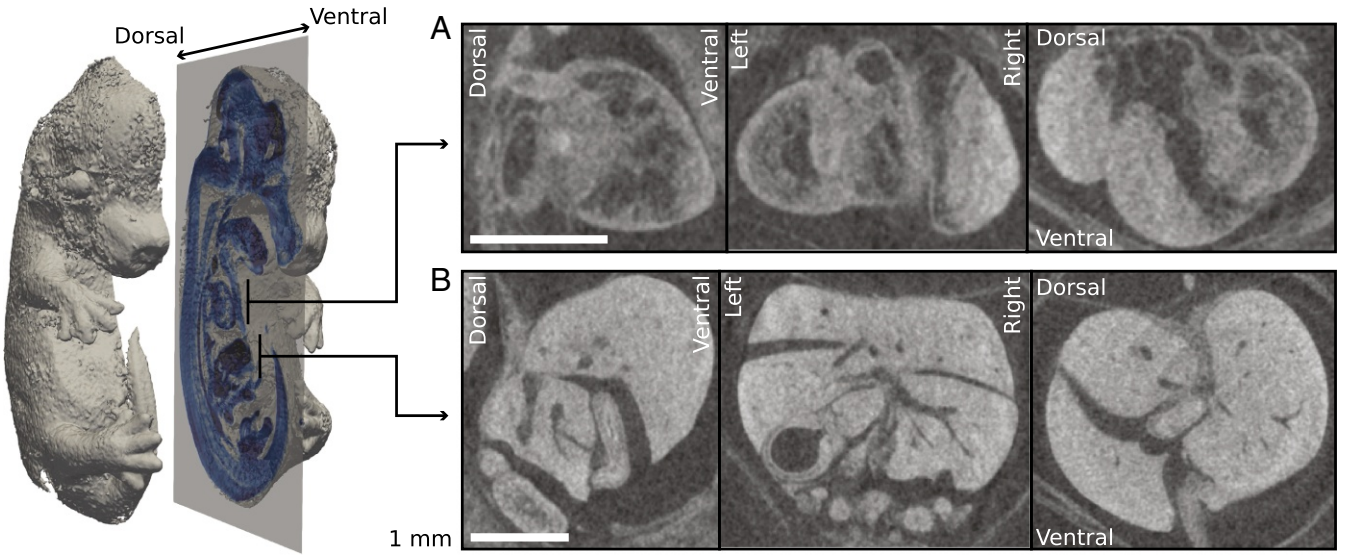

Fig. 4. An isosurface rendering of the reconstruction from the laser source is depicted in gray. A sagittal slice of the reconstruction is overlaid in blue. Enlarged sections of sagittal, coronal, and transverse slices around the heart and liver are plotted in *A* and *B*, respectively. (Scale bars, 1 mm.)

The X-ray parameters measured in this experiment are compared with previous laser-betatron results (7, 11, 19–21) in Fig. 5. As a guide to the applicability of the source for biological imaging we indicated the regions of the plot where the number of photons reaching each pixel of a standard detector would be 1, 10, and 100 through 1 cm of water. The considerable leap in average X-ray flux in the tens of kiloelectronvolts photon energy range shows that the source now operates in a regime suitable for imaging larger samples such as biopsies and small animals.

Further improvements to the laser-betatron apparatus are needed for it to be used as a dedicated bioimaging resource. First, although the X-ray source size is exceptionally small, inferred from measured X-ray beam parameters to be of order 1 μm, the imaging resolution was detector limited to $(78/M)$ μm by the properties of the scintillator (42). This could be improved by using a thinner scintillator viewed through a high-magnification optical system as is routinely used at synchrotrons to achieve micrometer-level resolution (43). The drawback of this approach is a lower X-ray to optical conversion efficiency and a smaller field of view. This may lead to a requirement for multiple-shot exposures, resulting in longer scan times. Second, despite the ability to capture images with a single pulse, the scan time was several hours because of a low laser repetition rate (0.05 Hz). This can be resolved by upgrading the laser system driving the accelerator. High-power laser technology is a growing industry and increasing commercialization is leading to more robust and compact products and a reduction in cost. Laser systems able to drive a betatron source at a multihertz repetition rate are already operational (44) and are affordable enough to install at multiple locations rather than being restricted to national facilities. Few-minute [1 frame per second (f.p.s.)] laser-betatron μCT has recently been achieved (45) and we do not see any technical barrier to conducting much faster tomographic scans (10–100 f.p.s.) with existing laser technology. The dose is low enough to perform longitudinal studies on small animals and a 10-Hz repetition rate is high enough to capture fast cyclic processes such as heartbeats and respiration. For embryonic imaging in particular, this capability could enable in utero X-ray imaging to visualize gestation stages in vivo that are not accessible by optical methods (24) and at better resolution than MRI (46) or ultrasound (47). With these developments the laser-betatron source should be able to reach photon fluxes $\sim 10^{10}$ ph·s^{-1}·mrad^{-2} in the near future. There is therefore an opportunity to implement this alternative technology to provide compact X-ray sources for rapid imaging of soft tissue biological samples with exceptional resolution.

Materials and Methods

Laser Wakefield Accelerator. The experiment was performed using the Gemini laser at the Science and Technology Facilities Council (STFC) Rutherford Appleton Laboratory. Pulses with energy 10.4 ± 0.5 J and 50 fs FWHM duration were focused using an *f*/40 spherical mirror to a peak intensity (6.3 ± 0.6) × 10^{18} W·cm^{-2} into a helium gas cell with a length variable between 3 mm and 42 mm. The density and length were scanned to find optimum conditions for stable, high-flux betatron beams, which occurred at a density of (2.6 ± 0.3) × 10^{18} cm^{-3} and a length of 20 mm. Electrons were deflected from the laser axis, using a 420-mm–long 0.95-T dipole magnet onto two calibrated Gd2O2S:Tb (Lanex) scintillator screens imaged with 16-bit optical cameras to measure the electron spectrum. In the preferred regime for betatron emission the spectrum comprised two components: a high-energy peak above 1.5 GeV and a lower-energy peak near 700 MeV. The total charge in the beam above 200 MeV was above 300 pC on 38% of shots.

X-Ray Characterization. The X-ray detector was a 150-μm–thick structured CsI scintillator fiber-coupled to a 2,048 × 2,048-pixel CCD camera placed 480 mm from the vacuum window. The pixel size was 13.5 × 13.5 μm, giving

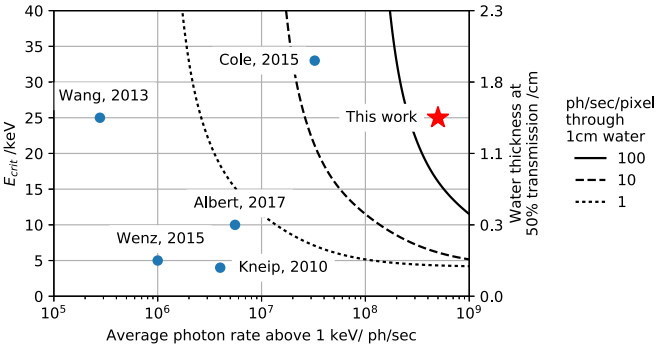

Fig. 5. The average photon flux and characteristic energy of the X-ray source described here in comparison with previous results on laser-betatron X-ray sources (7, 11, 19–21). The lines represent the incident photon flux on a typical 4-MP detector after passing through 1 cm of water, assuming the X-ray beam fills the detector.

an angular acceptance of 7.8 mrad. To determine photon flux, the camera was absolutely calibrated using a ^{55}Fe source. The X-ray spectrum was inferred by matching the measured transmission of the X-ray beam through an array of metal filters with that calculated for a trial on-axis synchrotron spectrum,

$$\frac{d^2I}{dEd\Omega} \propto \gamma^2\xi^2\mathcal{K}^2_{2/3}(\xi),$$

where $\xi = E/2E_{crit}$, the critical energy $E_{crit} = 3\hbar\gamma^2\omega_p^2 r_\beta/(4c)$, γ is the electron Lorentz factor, ω_p is the plasma frequency, r_β is the electron betatron oscillation radius, and $\mathcal{K}$ is a modified Bessel function of the second kind. The best-fit E_{crit} during the first 300 shots of the scan was 18 $\pm$ 1 keV. With knowledge of E_{crit} and $\omega_p \approx 9 \times 10^{13}$ rad s^{-1}, r_β is found to be of order 500 nm. The X-ray source size is estimated as $2r_\beta \sim 1\mu$m. On-shot spectral measurements were made by placing sets of filters in the four corners of the image.

X-Ray Imaging Beamline. The imaging samples were mounted on a compact rotation stage inside a sealed sample chamber, maintained at atmospheric pressure inside the main vacuum chamber. The entrance and exit windows were 50-μm polyimide foils. To prevent sample damage, the laser pulse was reflected after the exit of the gas cell by a 25-μm–thick polyimide foil acting as a plasma mirror. Two fixed 12-μm Al foils were placed in front of the sample chamber for protection and these also blocked X-ray photons with energy below 5 keV. The electron beam deflection in the magnetic spectrometer strongly reduced bremsstrahlung noise on the X-ray beam axis. After the sample chamber the X-ray beam exited the main vacuum chamber through a 250-μm–thick polyimide window and propagated through air to the detector.

X-Ray Beam Dosimetry. To measure X-ray dose a sheet of EBT3 radiochromic film was wrapped in 12-μm Al foil and placed in front of the sample chamber. One layer of the protective Al was removed so that the film received a dose equivalent to the sample dose. To avoid the risk of laser beam back reflection, the film was angled at 20° to the incoming beam—this was accounted for in the analysis. The film was irradiated with 100 X-ray pulses and then scanned as a 48-bit RGB (red, green, blue) TIFF image at 300 dpi resolution, using an Epson Expression 10000XL flatbed scanner 24 h postexposure (48). Absolute dosimetry was performed following the recommendations of the report of the American Association of Physicists in Medicine (AAPM) Task Group 61 (49) with the EBT3 film calibrated using a 220-kV X-ray tube (half-value layer of 0.79 mm of Cu) and a calibrated ionization chamber (NE2581; Thermo). The resulting 2D dose was calculated using optical density (OD) of the red channel and corrected using the corresponding OD of the blue channel in conjunction with the calibration curve (48) and then averaged over a 10×10-mm^2 field centered on the peak dose. In addition to the increase in OD in the exposed region (Fig. 2*D*), there was an unexpected increase in OD across the entire film leading to a background offset, which if produced by X-rays would correspond to a dose of $\approx$0.04 Gy. However, this is likely to be from light contamination, especially as parts of the film had been exposed to laser light. This offset has been subtracted from quoted dose values.

Image Analysis and Reconstruction. Noise in the laser-betatron images arises from Poisson photon noise, hot pixels caused by high-energy bremsstrahlung photons, and noise from the scintillator due to a compounding of Poisson effects. The images were processed first by correcting exceptionally bright pixels with an estimated value from the surrounding image using a selective median filter and then by applying a non–local-means denoising technique (50), which is able to reduce the noise level without compromising spatial resolution, as is the case for simpler convolutional filters. Pulse-to-pulse variations in the X-ray beam profile were accounted for by removing the region of the image containing the sample for each acquisition and infilling from the rest of the image. The acquired image was then divided by this estimate of the beam profile to recover a map of sample transmission. The spatial resolution of the scintillator was estimated from the edge-spread function of one of the metal filters. By fitting a smooth background behind the filter to eliminate the nonuniformity in the X-ray beam profile, the (assumed isotropic) point-spread function was found by fitting a Gaussian to the spatial derivative of the edge-spread function. SNR was measured by quantifying the random noise compared with the X-ray beam brightness across the image in 5×5-pixel windows. This was found to be $\approx$20 in the raw image and $\approx$100 after image processing. The peak SNR outside the sample is near the physical limit given the available flux. Ring artifacts and fluctuations in transmission between shots were filtered in the sinogram domain using a wavelet decomposition technique (51), before reconstruction using filtered back projection. For the laser-betatron scan, the X-ray source was of sufficiently low divergence that it was acceptable to use a parallel-beam reconstruction algorithm. The images and reconstructions shown in Fig. 3 have been sharpened using $I_{sharp} = B_3(I) + 30(B_3(I) - B_1(B_3(I))$, where $B_x(\cdot)$ represents a Gaussian blurring operation using a kernel of SD x pixels. The original images are available in *SI Appendix*, Fig. S3.

Commercial μCT Scanner. The μCT of the sample displayed in Fig. 3*D* was acquired using a Skyscan 1172 scanner (Bruker) with source size <5 μm. The X-ray source was operated at 70 kVp and 141 μA with a 0.5-mm aluminum filter. The detector was a 4,000 $\times$ 2,672-pixel CCD coupled to a scintillator, with an effective pixel size of 4.9 μm (1.8$\times$ magnification). Samples were rotated 180° around the vertical axis with a 0.5° step size and a 4-s exposure time ($\sim 5 \times 10^9$ photons per image) generating 399 projections in 2 h. Frame averaging was set to 2 and random movement to 10. To compare with the laser-betatron reconstruction, a subset of 360 images was selected, covering a rotation angle of 180°. The reconstruction was performed using a cone-beam algorithm provided by the NRecon software associated with the scanner. The resulting 3D dataset consists of a 4,000 $\times$ 4,000 $\times$ 2,000-voxel array, with each cubic element of the same linear dimension as the CCD pixels.

Sample Preparation. Mice were produced and housed in the Mary Lyon Center, MRC Harwell Institute, under specific opportunistic pathogen-free (SOPF) conditions. Individually ventilated cages adhering to environmental conditions as outlined in the Home Office Code of Practice were used. All animal studies were licensed by the Home Office under the Animals (Scientific Procedures) Act 1986 Amendment Regulations 2012 (SI 4/2012/3039), United Kingdom, and additionally approved by the Institutional Ethical Review Committee. C57Bl/6N mice were mated and detection of a vaginal plug the following morning was considered to be 0.5 dpc. At 14.5 dpc pregnant females were killed by cervical dislocation and the uterine horns dissected out. Individual embryos were removed from placentas and allowed to bleed out in cold PBS for $\sim$10 min. Embryos were placed in individual wells of a 12-well plate and fixed in 2 mL of 4% paraformaldehyde (PFA), pH 8, on a rocker at 4 °C for 24 h. Following fixation, embryos were stored in PBS, pH 8, until ready for potassium triiodide (Lugol) staining. Embryos were placed in individual glass bijou bottles with 20 mL of contrast agent, 50% Lugol solution (32922; Sigma-Aldrich) made up in distilled water (dH_2O). These were wrapped in foil to protect from light and placed on a rocker at room temperature for 2 d. Following contrast samples were rinsed and then washed with dH_2O for at least 1 h to remove any excess contrast solution. Samples were then embedded in 1% Iberose–high-specification agarose (AGR-500; Thistle Scientific). Samples were left to set in the agarose for a minimum of 2 h at room temperature before scan initiation.

ACKNOWLEDGMENTS. The authors gratefully acknowledge the Central Laser Facility staff for assistance during the experiment and A. Landman for helpful discussions. This research was supported by the Science and Technology Facilities Council (STFC) (ST/J002062/1, ST/P000835/1), the National Institute for Health (Grant U42OD011174), Medical Research Council (MRC) International Mouse Phenotyping Consortium (IMPC) Strategic Award 53658 (to L.T.), MRC Award MC_U142670370 (to D.P.N.), and funding from the MRC Strategic Partnership (MC-PC-12004) for the Cancer Research UK (CRUK)/MRC Institute for Radiation Oncology. G.S. and J.R.W. acknowledge support from the Engineering and Physical Sciences Research Council (EPSRC) (Grants EP/P010059/1 and EP/N027175/1).

1. Mangles SPD, et al. (2004) Monoenergetic beams of relativistic electrons from intense laser-plasma interactions. *Nature* 431:535–538.
2. Geddes CGR, et al. (2004) High-quality electron beams from a laser wakefield accelerator using plasma-channel guiding. *Nature* 431:538–541.
3. Faure J, et al. (2004) A laser-plasma accelerator producing monoenergetic electron beams. *Nature* 431:541–544.
4. Tajima T, Dawson JM (1979) Laser electron accelerator. *Phys Rev Lett* 43:267–270.
5. Esarey E, Schroeder CB, Leemans WP (2009) Physics of laser-driven plasma-based electron accelerators. *Rev Mod Phys* 81:1229–1285.
6. Kneip S, et al. (2009) Near-GeV acceleration of electrons by a nonlinear plasma wave driven by a self-guided laser pulse. *Phys Rev Lett* 103:035002.

7. Wang X, et al. (2013) Quasi-monoenergetic laser-plasma acceleration of electrons to 2 GeV. *Nat Commun* 4:1988.
8. Kim HT, et al. (2013) Enhancement of electron energy to the multi-GeV regime by a dual-stage laser-wakefield accelerator pumped by petawatt laser pulses. *Phys Rev Lett* 111:1–5.
9. Leemans WP, et al. (2014) Multi-GeV electron beams from capillary-discharge-guided subpetawatt laser pulses in the self-trapping regime. *Phys Rev Lett* 113:245002.
10. Rousse A, et al. (2004) Production of a keV X-ray beam from synchrotron radiation in relativistic laser-plasma interaction. *Phys Rev Lett* 93:135005.
11. Kneip S, et al. (2010) Bright spatially coherent synchrotron X-rays from a table-top source. *Nat Phys* 6:980–983.
12. Corde S, et al. (2013) Femtosecond x rays from laser-plasma accelerators. *Rev Mod Phys* 85:1–48.
13. Ta Phuoc K, et al. (2007) Demonstration of the ultrafast nature of laser produced betatron radiation. *Phys Plasmas* 14:080701.
14. Plateau GR, et al. (2012) Low-emittance electron bunches from a laser-plasma accelerator measured using single-shot x-ray spectroscopy. *Phys Rev Lett* 109:064802.
15. Albert F, Thomas AGR (2016) Applications of laser wakefield accelerator-based light sources. *Plasma Phys Controlled Fusion* 58:103001.
16. Kneip S, et al. (2011) X-ray phase contrast imaging of biological specimens with femtosecond pulses of betatron radiation from a compact laser plasma wakefield accelerator. *Appl Phys Lett* 99:093701.
17. Fourmaux S, et al. (2011) Single shot phase contrast imaging using laser-produced betatron x-ray beams. *Opt Lett* 36:2426–2428.
18. Najmudin Z, et al. (2014) Compact laser accelerators for x-ray phase-contrast imaging. *Philos Trans R Soc A* 372:20130032.
19. Cole JM, et al. (2015) Laser-wakefield accelerators as hard x-ray sources for 3D medical imaging of human bone. *Sci Rep* 5:13244.
20. Wenz J, et al. (2015) Quantitative X-ray phase-contrast microtomography from a compact laser-driven betatron source. *Nat Commun* 6:7568.
21. Albert F, et al. (2017) Observation of betatron x-ray radiation in a self-modulated laser wakefield accelerator driven with picosecond laser pulses. *Phys Rev Lett* 118:134801.
22. Metscher BD (2009) MicroCT for comparative morphology: Simple staining methods allow high-contrast 3D imaging of diverse non-mineralized animal tissues. *BMC Physiol* 9:11.
23. Adams D, et al. (2013) Bloomsbury report on mouse embryo phenotyping: Recommendations from the IMPC workshop on embryonic lethal screening. *Dis Model Mech* 6:571–579.
24. Singh M, et al. (2016) Applicability, usability, and limitations of murine embryonic imaging with optical coherence tomography and optical projection tomography. *Biomed Opt Express* 7:2295–2310.
25. Bravin A, Coan P, Suortti P (2013) X-ray phase-contrast imaging: From pre-clinical applications towards clinics. *Phys Med Biol* 58:R1–R35.
26. Dickinson ME, et al. (2016) High-throughput discovery of novel developmental phenotypes. *Nature* 537:508–514.
27. Meehan TF, et al. (2017) Disease model discovery from 3,328 gene knockouts by the international mouse phenotyping consortium. *Nat Genet* 49:1231–1238.
28. Laforce B, et al. (2017) Integrated three-dimensional microanalysis combining X-ray microtomography and X-ray fluorescence methodologies. *Anal Chem* 89:10617–10624.
29. du Plessis A, et al. (2017) Laboratory x-ray micro-computed tomography: A user guideline for biological samples. *GigaScience* 6:1–11.
30. Fourmaux S, et al. (2011) Demonstration of the synchrotron-type spectrum of laser-produced Betatron radiation. *New J Phys* 13:033017.
31. Aufrichtig R, Xue P (2000) Dose efficiency and low-contrast detectability of an amorphous silicon x-ray detector for digital radiography. *Phys Med Biol* 45:2653–2669.
32. Clark D, Badea C (2014) Micro-CT of rodents: State-of-the-art and future perspectives. *Phys Med* 30:619–634.
33. Voide R, et al. (2009) Time-lapsed assessment of microcrack initiation and propagation in murine cortical bone at submicrometer resolution. *Bone* 45:164–173.
34. Pacureanu A, Langer M, Boller E, Tafforeau P, Peyrin F (2012) Nanoscale imaging of the bone cell network with synchrotron x-ray tomography: Optimization of acquisition setup. *Med Phys* 39:2229–2238.
35. Hieber SE, et al. (2016) Tomographic brain imaging with nucleolar detail and automatic cell counting. *Sci Rep* 6:32156.
36. Chang S, et al. (2015) Synchrotron x-ray imaging of pulmonary alveoli in respiration in live intact mice. *Sci Rep* 5:8760.
37. Mokso R, et al. (2015) Four-dimensional in vivo X-ray microscopy with projection-guided gating. *Sci Rep* 5:8727.
38. Larsson DH, Vågberg W, Yaroshenko A, Yildirim AO, Hertz HM (2016) High-resolution short-exposure small-animal laboratory x-ray phase-contrast tomography. *Sci Rep* 6:39074.
39. Eggl E, et al. (2016) The Munich compact light source: Initial performance measures. *J Synchrotron Radiat* 23:1137–1142.
40. Eggl E, et al. (2015) X-ray phase-contrast tomography with a compact laser-driven synchrotron source. *Proc Natl Acad Sci USA* 112:5567–5572.
41. Gradl R, et al. (2017) Propagation-based phase-contrast X-ray imaging at a compact light source. *Sci Rep* 7:4908.
42. Larsson JC, Lundström U, Hertz HM (2016) Characterization of scintillator-based detectors for few-ten-keV high-spatial-resolution x-ray imaging. *Med Phys* 43:2731–2740.
43. Stampanoni M, et al. (2006) Trends in synchrotron-based tomographic imaging: The SLS experience. *Dev X-Ray Tomography V* 6318:63180M.
44. Danson C, Hillier D, Hopps N, Neely D (2015) Petawatt class lasers worldwide. *High Power Laser Sci Eng* 3:e3.
45. Döpp A, et al. (2018) Quick x-ray microtomography using a laser-driven betatron source. *Optica* 5:199–203.
46. Parasoglou P, Berrios-Otero CA, Nieman BJ, Turnbull DH (2013) High-resolution MRI of early-stage mouse embryos. *NMR Biomed* 26:224–231.
47. Li Y, et al. (2015) Global genetic analysis in mice unveils central role for cilia in congenital heart disease. *Nature* 521:520–524.
48. ISP (2009) Gafchromic EBT2 self-developing film for radiotherapy dosimetry, Revision 1, Technical Report. Available at www.veritastk.co.jp/attached/2062/GAFCHROMICEBT2TechnicalBrief-Rev1.pdf. Accessed May 24, 2018.
49. Chair CM, et al. (2001) AAPM protocol for 40–300 kV x-ray beam dosimetry in radiotherapy and radiobiology. *Med Phys* 28:868–893.
50. Buades A, Coll B, Morel JM (2005) A review of image denoising algorithms, with a new one. *SIAM J Multi Model Sim* 4:490–530.
51. Münch B, Trtik P, Marone F, Stampanoni M (2009) Stripe and ring artifact removal with combined wavelet-Fourier filtering. *Opt Express* 17:8567–8591.